Interface-engineered atomically thin Ni_3S_2/MnO_2 heterogeneous nanoarrays for efficient overall water splitting in alkaline media

Ye Xiong, Lulu Xu, Chunde Jin, Qingfeng Sun*

School of Engineering, Zhejiang A & F University, Hangzhou, Zhejiang Province, 311300, PR China

ARTICLE INFO

ABSTRACT

Designing bifunctional non-noble metal electrocatalysts with excellent hydrogen and oxygen evolution performances is a promising candidate for sustainable generation of renewable and clean hydrogen energy. Herein, an atomically thin Ni_3S_2/MnO_2 heterogeneous nanoarray located on Ni foam (NF-Ni_3S_2/MnO_2) is developed for overall water splitting. The construction strategy involves a simple two-step hydrothermal conversion, and the morphology and composition of the hybrid nanoarray can be easily customized. The fabricated NF-Ni_3S_2/MnO_2 with a certain exposed interface and active sites perfectly integrated and optimized the advantages of both several layered Ni_3S_2 and MnO_2, realizing the desired fast kinetics and outstanding performance for overall water splitting in alkaline media. Consequently, the constructed NF-Ni_3S_2/MnO_2 reveals a low overpotential (η_{10}) of 102 mV and 260 mV at a 10 mA cm^{-2} current density in 1.0 M KOH for HER and OER, respectively. Moreover, it achieves a current density of 10 mA cm^{-2} at a low voltage of only 1.52 V throughout the overall water splitting, which is outperforming the currently reported Pt/C-IrO_2/C couple. Furthermore, density functional theory calculations evidence that the excellent total hydrolysis of NF-Ni_3S_2/MnO_2 is attributed to the hierarchical heterointerfaces, which results in effective adsorption and cleavage of H_2O molecule on the catalyst surface.

1. Introduction

Clean and sustainable electrocatalytic water splitting technology is often considered the most promising approach to solving the issues of energy consumption and environmental pollution [1–3]. However, the overall water splitting efficiency of most electrocatalysts is usually affected somewhat by the inescapable dynamic overpotential in the hydrogen and oxygen evolution reaction (HER and OER), where the lowest thermodynamic potential for HER and OER is about 1.23 V [4–7]. Especially, the energy-intensive anodic OER related to the transfer of four-electron as well as the generation of O−O bond during the four protons removal has severely constrained the efficiency of water electrolysis [8–11]. Moreover, as the most efficient HER/OER catalysts, the large-scale development of noble-metal platinum/ruthenium/iridium-based materials are always hindered by their high expense and low earth resources [12,13]. In addition, in view of this fact, most electrode materials are easily corroded in acid conditions, and alkaline water electrolysis is widely adopted in the industry [14,15]. Therefore, designing superior bifunctional non-noble metal alkaline electrocatalysts having compatibility and comprehensive properties for both HER and OER is necessary.

Due to the unique interlayer structure, two-dimensional (2D) materials such as transition metal oxides, sulfides, and phosphides exhibit great application prospects in photo/electrocatalytic water decomposition [16–18]. For example, non-precious metal nickel (Ni) is considered to be an important substitute for precious metal platinum in view of its low cost, high availability and excellent HER activity, and has been widely studied for alkaline water electrolysis [8,19–21]. Moreover, attributing to the unique electronic structure that totally different to their corresponding bulk noumenal material, defect engineering constructed half-metallic 2D transition metal nanosheets with one or several atomic layer thicknesses are significantly utilized for high-efficient photo/electro-catalysis [22]. For instance, Zhao et al. realize the efficient overall water splitting in an alkaline environment via defect-engineered ultrathin δ-MnO_2 nanosheet arrays [23]. Furthermore, owing to its heterogeneous nanostructures, the two-phase heterogeneous electrocatalyst exhibits synergistic kinetics at various active sites and electronic configuration interfaces relative to a single homogeneous catalyst. Correspondingly, Yang et al. confirm that a current density of 10 mA cm^{-2} for HER and OER is displayed at a low overpotential (η_{10}) of 98 and 249 mV by the interface engineering fabricated MoS_2-Ni_3S_2 heterojunction [24]. In addition, ascribing to the

---

* Corresponding author.
E-mail address: qfsun@zafu.edu.cn (Q. Sun).

excellent corrosion resistance and high water decomposition rate, transition metal heterogeneous materials and the like are considered to be the most promising alternative to alkaline electrocatalytic materials. Hence, the use of interface engineering to construct a novel 2D ultrathin heterogeneous composite seems to be an eye-catching method to improve the overall water decomposition of transition metal-based catalysts.

Although two-dimensional transition manganese-based oxides have high earth abundance and easy-regulated structure and morphology, they are greatly hindered in the application of electrocatalytic water splitting due to their inappropriate electronic structure and low conduction band levels. To optimize the catalytic activity of MnO_2, herein, an intertwined 2D atomically thin Ni_3S_2/MnO_2 biphasic nanoarray was successfully fabricated via a simple two-step in situ hydrothermal conversion using Ni foam (denoted as NF) as a template. The well-designed NF-Ni3S$_2$/MnO$_2$ hetero-arrays possessed a modified conductivity and a certain exposed interface and active sites, achieving the inheritance and optimization of single/double layered Ni_3S_2 nanosheets and δ-MnO_2 nanosheets. Therefore, a comparable HER and OER activity and stability were obtained than the benchmark commercial Pt and Ir based catalysts. It is worth noting that the obtained NF-Ni$_3$S$_2$/MnO$_2$ heterogeneous catalyst was capable of achieving a high current density of $10\ mA\ cm^{-2}$ at an applied voltage of only 1.52 V throughout the overall water splitting. More importantly, the construction and activation mechanism of Ni_3S_2/MnO_2 heterojunction for overall water decomposition was proposed, which is significant for the development and application of Ni-Mn based electrocatalysts.

2. Experimental section

2.1. Materials

Chemicals were analytical grade and purchased from commercial sources. Thioacetamide (TAA), potassium permanganate ($KMnO_4$), ethanol (EtOH), acetone (ACE) and hydrochloric acid (HCl) were obtained from Aladdin. Metal Ni foam (NF) was buy from Hefei Ke Jing Materials Technology Co. LTD. And, the commercial Pt/C (20 wt%) and IrO_2/C (20 wt%) were provided by Alfa Aesar.

2.2. Preparation of catalysts

Prior to use, the NF (4 cm × 2 cm) was first pretreated with a mixture of acetone and ethanol (volume ratio 1:1) under ultrasonication for 20 min, next immersed into a 2.5 M HCl solution for 30 min, then cleaned with ultrapure water and dried at 50 °C for 20 h. The quality of the cleaned NF was 0.257 g.

The NF-Ni$_3$S$_2$/MnO$_2$ nanoarray was fabricated by a two-step hydrothermal method. In the typical synthesis, 2.5 mmol of $KMnO_4$ was dissolved in 30 mL of deionized water under magnetic stirring, and then transferred into a 50 mL autoclave with Teflon liner. Followed, a piece of the as-pretreated NF was immersed in the solution, and the autoclave was kept at 100 °C for 16 h. During the hydrothermal treatment, an associated redox reaction would be occurred between the Ni metal and MnO_4^-, according to Eq. (1). Accordingly, the obtained product was marked as NF-Ni(OH)$_2$/MnO$_2$. Next, NF-Ni(OH)$_2$/MnO$_2$ would be further treated with a certain amount of TAA in an autoclave. After hydrothermal treatment at 120 °C for 8 h, NF-Ni$_3$S$_2$/MnO$_2$ was generated. The feed mass of TAA ranged from 1 to 5 mmol to regulate the heterostructure and composition of NF-Ni$_3$S$_2$/MnO$_2$.

$$3Ni + 2\,MnO_4^- + 4H_2O = 2MnO_2 + 3Ni(OH)_2 + 2OH^- \tag{1}$$
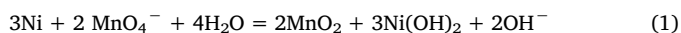
Pure NF-Ni$_3$S$_2$ was prepared similarly to NF-Ni$_3$S$_2$/MnO$_2$. In brief, the cleaned NF was immersed in a 100 mL Teflon- reaction vessel having 50 mL of 3 mmol TAA aqueous solution and kept at 120 °C for 8 h. The obtained product was cleaned with water and oven drying at

50 °C for 20 h, marking as NF-Ni$_3$S$_2$ material.

2.3. Characterization

X-ray diffraction (XRD) patterns were collected with a Bruker D8 Focus X-ray diffractometer using Cu Kα radiation (λ = 1.5405 Å) and a 2°/min scan rate. Sample morphologies were characterized using a JEM-2100 F transmission electron microscope (TEM) and a Hitachi S-4800 field emission scanning electron microscope (SEM) equipped with an energy dispersive spectrometer (EDS). X-ray photoelectron spectroscopy (XPS) data were collected on a VGESCALABMKII X-ray photoelectron spectrometer using a non-monochromatized Al-Kα X-ray source, and binding energies were calibrated against the C1s signal at 284.60 eV of adventitious hydrocarbons. The thickness of nanosheets was determined by atomic force microscopy (AFM) (Bruker multimode 8). Nitrogen adsorption-desorption isotherms were measured at 77 K with a Micromeritics ASAP 2020 surface area and porosity analyzer (Micromeritics instrument Ltd., USA). All periodic first-principles calculations were performed using the spin-polarized density functional theory (DFT) implemented in the Vienna ab initio simulation package (VASP), as detailed in Supporting Information.

2.4. Electrochemical testing

The performance of HER or OER was evaluated by a three-electrode system of an electrochemical workstation. NF-Ni$_3$S$_2$/MnO$_2$, NF-Ni(OH)$_2$/MnO$_2$ and NF-Ni$_3$S$_2$ were custom made to be 1 cm × 1 cm and served as working electrodes. For powdered IrO_2/C and Pt/C, it was made into a homogeneous slurry (5 mg catalyst and 20 μL 5% PVDF were added into 1980 μL water/ethanol (v/v = 5:1) mixed solution) and then uniformly applied to the pretreated 1 cm^2 NF. Graphite rod was employed as the counter electrodes, while saturated Ag/AgCl electrode were and reference electrodes. Linear sweep voltammetry and cyclic voltammetry were performed at 1.0 M KOH at a scan rate of 1 mV s^{-1}. Reversible hydrogen electrode (RHE) scale was calculated by Eq. 2:

$$E_{RHE} = E_{Ag/AgCl} + 0.059pH + E^{\circ}_{Ag/AgCl} \tag{2}$$

Where, E_{RHE} was the converted potential vs. RHE, $E_{Ag/AgCl}$ was the experimentally measured potential against the Ag/AgCl reference electrode, and $E^{\circ}_{Ag/AgCl}$ was the standard potential of Ag/AgCl at 25 °C (0.197 V).

Electrochemical impedance spectra were performed under an open circuit potential from 0.01 to 100 KHz at an alternating current voltage amplitude of 5 mV. Electrochemical impedance spectroscopy is the result of automatic *i*R calibration of the electrochemical instrument.

3. Results

3.1. Fabrication and characterization of NF-Ni$_3$S$_2$/MnO$_2$

As shown in Fig. 1a, NF-Ni$_3$S$_2$/MnO$_2$ hetero-arrays were prepared via simple two-step hydrothermal conversion of NF with $KMnO_4$ and thioacetamide (TAA) in turn. First, ultrathin nickel manganese oxide (denoted as NF-Ni(OH)$_2$/MnO$_2$) hybrid nanosheet arrays were generated on NF surface under the redox between MnO_4^- and Ni metal. Next, upon further processing by TAA, surface Ni metal matrix of NF template and the previously formed Ni(OH)$_2$ would be vulcanized to Ni_3S_2 and intertwined with the prior MnO_2 nanosheets to produce the final NF-Ni$_3$S$_2$/MnO$_2$ hierarchical structure.

The morphology transformation of NF during the preparation process was recorded in detail by Scanning Electron Microscopy (SEM). As displayed in Fig. S1a–c, the smooth surface of NF became rougher as the transformation progresses, indicating the generation of more complex multilevel structures. This structure might imply that the formed NF-Ni$_3$S$_2$/MnO$_2$ possessed a higher specific surface area (S_{BET}) and more
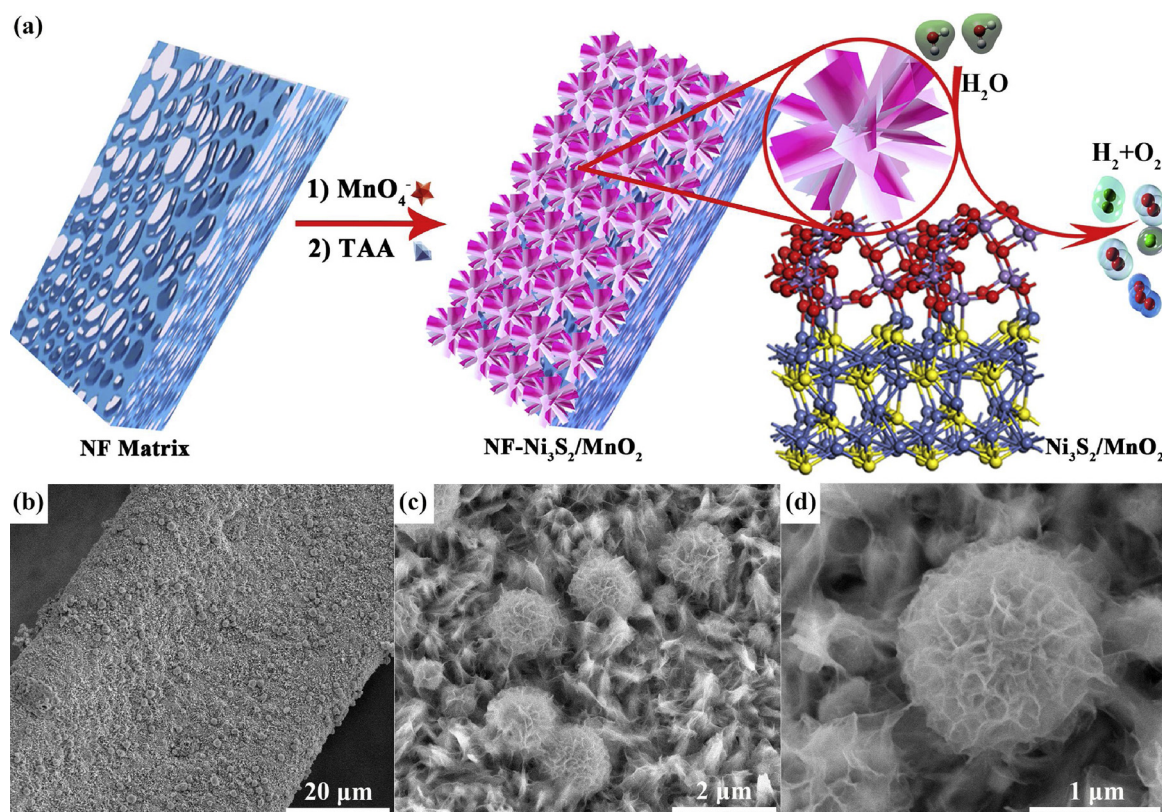
Fig. 1. (a) Schematic illustration of the preparation of NF-Ni$_3$S$_2$/MnO$_2$. (b–d) SEM images of NF-Ni$_3$S$_2$/MnO$_2$.

exposed heterogeneous interfaces or activated sites that advantageous for improving the catalytic activity of catalysts [25,26]. Fig. S1d–f were the SEM images of NF-Ni(OH)$_2$/MnO$_2$, in which Ni(OH)$_2$/MnO$_2$ microspheres composited of Ni(OH)$_2$/MnO$_2$ nanosheets were interwoven on the surface of 3D NF framework, forming a uniform array structure with 30–200 nm unevenness macro/mesopores. Correspondingly, the detection of Ni, Mn, K, and O elements on NF-Ni(OH)$_2$/MnO$_2$ surface by Energy Dispersive Spectrometer (EDS) in Fig. S2 enabled to demonstrate the generation of Ni(OH)$_2$/MnO$_2$. The minority K elements could be intercalating elements between the δ-MnO$_2$ layers [23,27,28]. However, a more intricate Ni$_3$S$_2$/MnO$_2$ hybrid array appeared after further vulcanization of NF-Ni(OH)$_2$/MnO$_2$. As exhibited in Figs. 1b–d and S3, it could be learned that a number of nanoflowers constituted by nanosheets were anchored and embedded in the interval of a relatively regular array of nanosheets. The lower layer of the regular array might be derived from the Ni on NF surface and the majority of Ni(OH)$_2$/MnO$_2$ microsphere array. Whereas, the upper nanoflowers are likely to be some pure Ni$_3$S$_2$/MnO$_2$ converted from the few single Ni(OH)$_2$/MnO$_2$ nanospheres. As evidenced by the relevant EDS spectra (Fig. S4), though both the two parts were made up by Ni, Mn, O, S, the molar ratio of Ni to Mn was obviously different (Table S1). The ratio of nanoflowers (8.64) on the up-layer was similar to the value in the NF-Ni(OH)$_2$/MnO$_2$ intermedium (8.71) but far less than that of the down-layer (20.05). This could be attributed to the overdose of TAA during the reaction, resulting in a large conversion of NF to Ni$_3$S$_2$ [24]. Additionally, the morphology of the NF-Ni$_3$S$_2$/MnO$_2$ array could be programmed by regulating the molar of TAA. As displayed in Fig. S5, a uniform array of NF-Ni$_3$S$_2$/MnO$_2$ was obtained when the molar of TAA was 2 mmol.

The corresponding nitrogen adsorption-desorption curves and pore distribution curves of the fabricated NF-Ni(OH)$_2$/MnO$_2$ and NF-Ni$_3$S$_2$/MnO$_2$ hetero-arrays were revealed in Fig. S6. Apparently, NF-Ni$_3$S$_2$/MnO$_2$ hybrid arrays had a higher S$_{BET}$ of 105.8 m^2 g^{-1} and an average pore size of 9.4 nm relative to pure NF-Ni(OH)$_2$/MnO$_2$ nanosheets

(57.2 m^2 g^{-1}, 18.2 nm). This result was greatly in agreement with the previous assumption on the structure. X-ray diffraction (XRD) analysis was performed to confirm the evolution of the crystal structure of the material during the two-step hydrothermal process. As displayed in Fig. S7, XRD patterns of NF-Ni(OH)$_2$/MnO$_2$, NF-Ni$_3$S$_2$/MnO$_2$, and pure NF-Ni$_3$S$_2$ (NF directly sulfide by TAA) demonstrated the effective conversion of Ni(OH)$_2$/MnO$_2$ to Ni$_3$S$_2$/MnO$_2$. Among them, NF-Ni$_3$S$_2$/MnO2 was perfectly matched with the combinations of δ-MnO$_2$ (JCPDS No. 86-0666) and Ni$_3$S$_2$ (JCPDS No. 44-1418) [29,30]. The diffraction peaks of NF-Ni$_3$S$_2$/MnO$_2$ at 12.2°, 25.1°, and 36.6° could be assigned to the (003), (006), and (101) phase of δ-MnO$_2$, while peaks at 21.8°, 31.1°, 37.8°, 38.3°, 44.3°, 49.4°, 50.3°, and 55.2° belonged to the (101), (110), (003), (021), (101), (113), (211) and (122) planes of the Ni$_3$S$_2$ crystal. In addition, it could be clearly found that the peaks of NF-Ni(OH)$_2$/MnO$_2$ were made up the δ-MnO$_2$ and hexagonal Ni(OH)$_2$ (PDF No. 14-0117) [31].

Transmission electron microscopy (TEM) was employed to investigate the interface relationship between Ni$_3$S$_2$ and MnO$_2$. As exhibited in Figs. 2a and S8, a clear intertwined NF-Ni$_3$S$_2$/MnO$_2$ heterogeneous array architecture that coincident with the SEM result was observed from the low-magnification TEM image. The interface relationship of Ni$_3$S$_2$ and MnO$_2$ was revealed by the corresponding high-resolution TEM (HRTEM) images of NF-Ni3S2/MnO$_2$, wherein two different lattice fringes were detected. As displayed in Fig. 2c, the lattice fringe with a 0.201 nm distance was assigned to the (202) lattice planes of Ni$_3$S$_2$, while another fringe having a 0.244 nm was appointed as the (101) plane of δ-MnO$_2$ [32,33]. Moreover, a disordered lattice region was found at the intersection of the two interfaces, which further confirmed the strong interfacial interaction between the (101) crystal plane of MnO2 and the (202) crystal plane of Ni3S2. As shown in Fig. 2b, several atomic thicknesses edge of NF-Ni3S2/MnO2 could be roughly seen from the HRTEM image. The value was confirmed to be about 1.3–1.6 nm by atomic force microscopy (AFM, Fig. 2d), which was approximately equal to the thickness of several atomic layers [23].
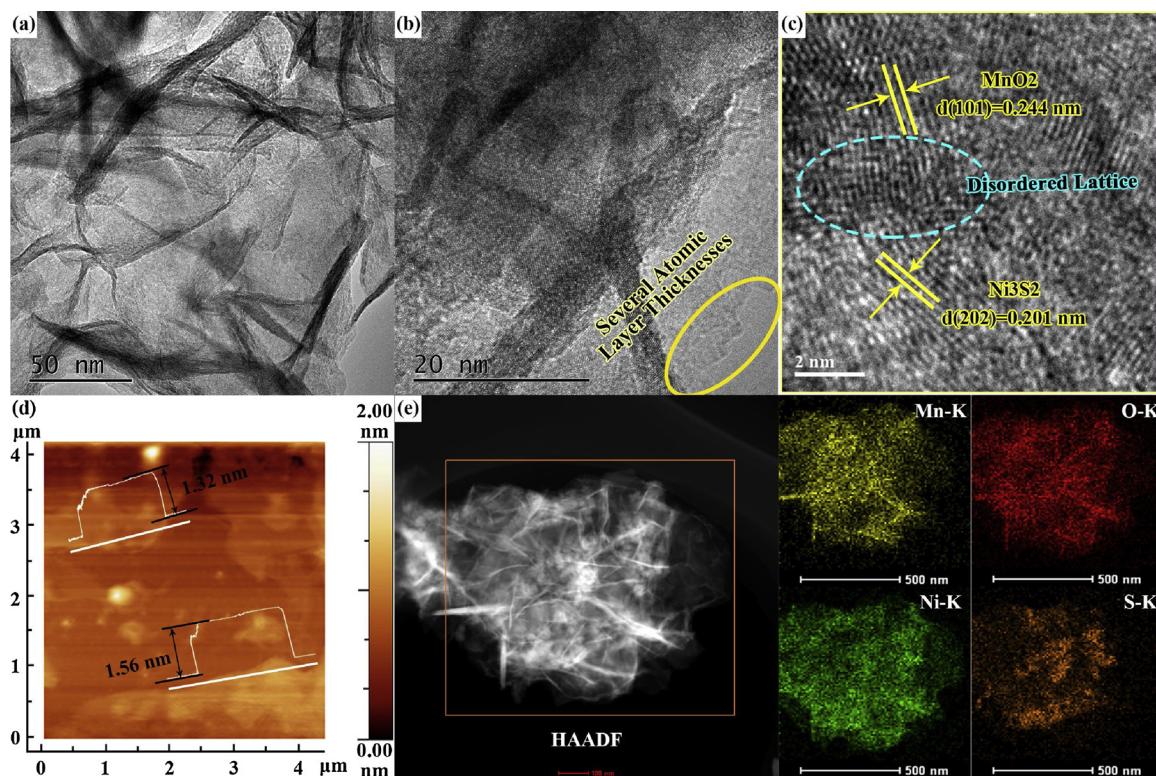
Fig. 2. (a–c) TEM images, (d) AFM images and (e) TEM mapping of the fabricated NF-Ni$_3$S$_2$/MnO$_2$ heterogeneous array.

As a comparison, TEM and AFM images of NF-Ni(OH)$_2$/MnO$_2$ intermediates were provided in Figs. S9 and S10. The edge size of NF-Ni3S2/MnO2 was also found to be close to several layers of atomic thickness, indicating that the sheet structure was perfectly inherited throughout the synthesis. The TEM Mapping of NF-Ni$_3$S$_2$/MnO$_2$ was presented in Fig. 2e, the uniform spatial distribution of Ni, Mn, S, and O elements indicated the efficient combination of the several-layered Ni3S2 and MnO2 nanosheets, which might contribute to a higher concentration of active sites and more reasonable electronic transmission channels [34,35]. Therefore, predicting that a superior electrocatalytic property than single Ni$_3$S$_2$ and MnO$_2$ arrays might be obtained. Additionally, the detailed TEM, AFM and TEM Mapping analysis of NF-Ni(OH)$_2$/MnO$_2$ and the pure NF-Ni$_3$S$_2$ was offered in Figs. S9–S11.

The surface composition and chemical valence of the NF-Ni$_3$S$_2$/MnO$_2$ hybrid were examined by X-ray photoelectron spectroscopy (XPS). The discovery of the Ni, Mn, O, and S elements in the full spectrum (Fig. 3a) were in good agreement with EDS results (Fig. S4). High-resolution Ni 2p spectra were presented in Fig. 3b. The two main strong peaks of NF-Ni$_3$S$_2$/MnO$_2$ with an energy gap of approximately 17.6 eV at 856.7 eV and 874.3 eV corresponded to Ni^{2+} 2p$_{3/2}$ and Ni^{2+} 2p$_{3/2}$, respectively [36,37]. While the weaker peaks at 862.6 eV and 880.6 eV could be assigned to other Ni$^-$ based satellite peaks or hydrated nickel oxide. Compared to the pure NF-Ni$_3$S$_2$, the slight positive shift of Ni 2p$_{3/2}$ signal (~0.9 eV) in NF-Ni$_3$S$_2$/MnO$_2$ might be owing to that the existence of strong electronic interactions between Ni$_3$S$_2$ and MnO$_2$, which suggested the successful establishment of coupling interfaces [8,36]. Similarly, the Mn^{3+} 2p$_{3/2}$ signal in NF-Ni$_3$S$_2$/MnO$_2$ (Fig. 3c) also revealed a movement toward high binding energy (~1.2 eV) in comparison with pure MnO$_2$ nanoparticles. This phenomenon further proved that the generation of Ni$_3$S$_2$ and MnO$_2$ heterojunction interfaces. Furthermore, the spectra of Mn 2p could be decomposed into two double peaks [38]. One double peak at 642.8 and 654.4 eV having an energy difference of about 11.7 eV were belonged to Mn^{3+} 2p$_{3/2}$ and Mn^{3+} 2p$_{1/2}$ in MnO$_2$, respectively. And, the rest was allocated to Mn^{4+} 2p$_{3/2}$ and Mn^{4+} 2p$_{1/2}$ of MnO$_2$, respectively. The

fine spectra of S 2p for NF-Ni$_3$S$_2$/MnO$_2$ were exhibited in Fig. 3d, in which the peaks at 162.3 eV and 163.6 eV enabled to be specified as S^{2-} 2p$_{3/2}$ and S^{2-} 2p$_{1/2}$, respectively [39]. To sum up, a hybrid NF-Ni$_3$S$_2$/MnO$_2$ nano-array with high-efficiency charge transport path and high concentration of reactive sites was successfully constructed.

3.2. Electrocatalytic performances of NF-Ni$_3$S$_2$/MnO$_2$

The HER activity of the NF-Ni$_3$S$_2$/MnO$_2$ electrode was examined in 1 M KOH aqueous electrolyte using a standard three-electrode system. For comparison, the HER performances of pure NF, NF-Ni$_3$S$_2$, NF-Ni(OH)$_2$/MnO$_2$, and commercial Pt/C were also conducted in same conditions. The polarization curves with iR correction of those samples were exhibited in Fig. 4a, in which Pt/C supported by NF revealed the best activity. For the as-prepared NF-Ni$_3$S$_2$/MnO$_2$, it displayed an extraordinary performance on HER compared to other contrast samples. It could be seen that the overpotentials (η) required at the current density (j) of 10 mA cm^{-2} (η_{10}) and 100 mA cm^{-2} (η_{100}) for NF-Ni$_3$S$_2$/MnO$_2$ were low to 102 mV and 197 mV, respectively. However, the η_{10} for NF, NF-Ni$_3$S$_2$, and NF-Ni(OH)$_2$/MnO$_2$ were as high as 324 mV, 192 mV, and 234 mV, respectively. The significant optimizing of NF-Ni$_3$S$_2$/MnO2 for HER demonstrated the cooperative reinforcement between MnO$_2$ nanosheets and Ni$_3$S$_2$ nanosheets. Moreover, the performance of NF-Ni$_3$S$_2$/MnO$_2$ on HER was also top-notch compared to other non-noble metal electrocatalysts (Table S2) [24,29,40–52]. Corresponding Tafel plots of these catalysts were shown in Fig. 4b, where a HER kinetics improvement consistent with the enhanced HER activity was found. In contrast to NF (η_{onset} = 254 mV, and b = 149 mV dec^{-1}), NF-Ni$_3$S$_2$ (η_{onset} = 124 mV, and b = 105 mV dec^{-1}), and NF-Ni(OH)$_2$/MnO$_2$ (η_{onset} = 169 mV, and b = 120 mV dec^{-1}), the lowest onset overpotential (η_{onset} = 43 mV) and Tafel slope (b = 69 mV dec^{-1}) of NF-Ni$_3$S$_2$/MnO$_2$ delivered that the hydrogen yield rate increased rapidly with the application of an overpotential, corresponding to the high activity reflected in the polarization curves.

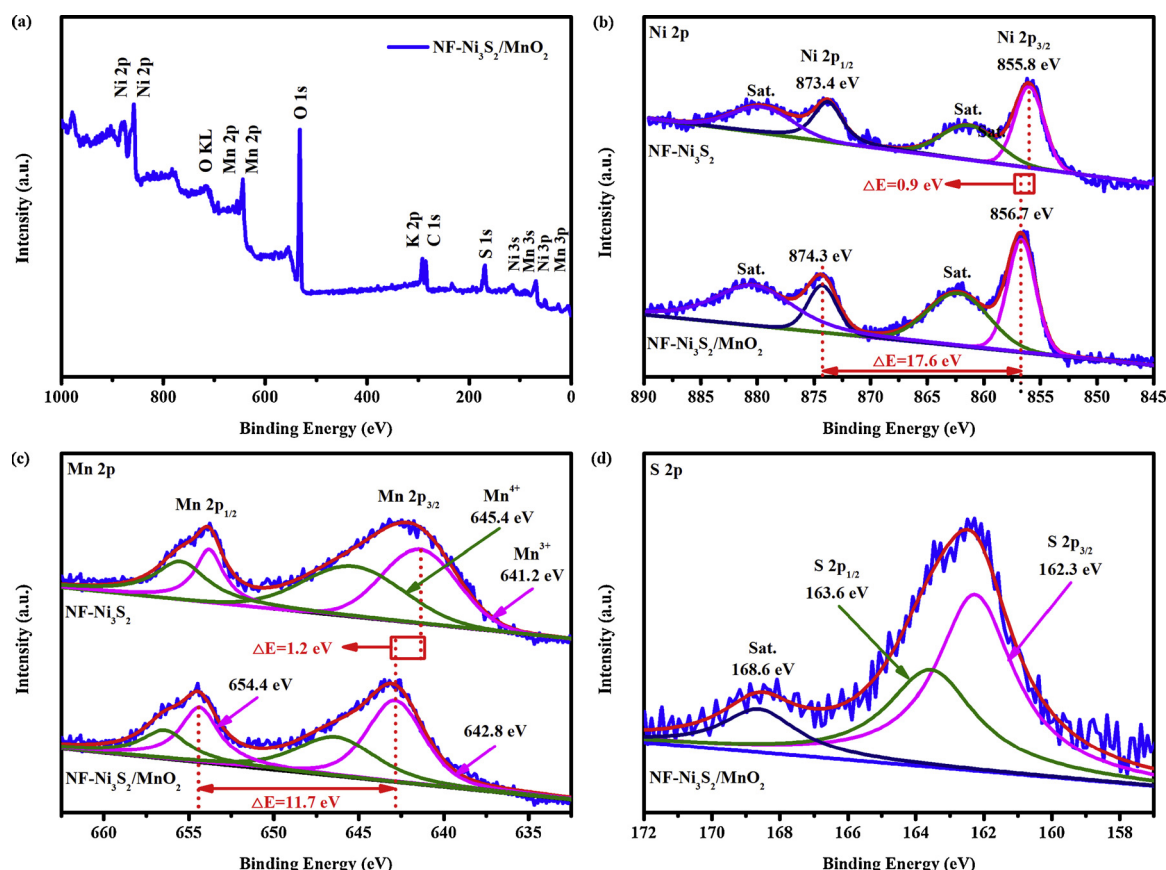As an important means to evaluate the catalytic activity of

Fig. 3. XPS spectra of NF-Ni$_3$S$_2$/MnO$_2$. (a) Full spectrum, (b) Ni 2p fine spectrum, (c) Mn 2p fine spectrum, and (d) S 2p fine spectrum.

electrocatalysts, electrochemical surface areas (ECSAs) of these samples originated from the cyclic voltammograms (CVs) were presented in Fig. S12. The double-layer capacitances (C_{dl}) of NF-Ni$_3$S$_2$/MnO$_2$ in 1.0 M KOH arrived at 118.3 mF cm^{-2} (Fig. 4c), which was apparently higher than that of NF-Ni$_3$S$_2$ (41.2 mF cm^{-2}) and NF-Ni(OH)$_2$/MnO$_2$ (37.4 mF cm^{-2}). The high C_{dl} value implied that NF-Ni$_3$S$_2$/MnO$_2$ had a concentrated active site for HER, which was in good agreement with the roughness and S$_{BET}$ of NF-Ni$_3$S$_2$/MnO$_2$. As shown in Fig. S13, a normalized electrocatalytic currents was conducted to deep analyze the intrinsic activity. Obviously, the bigger value (j) of NF-Ni$_3$S$_2$/MnO$_2$ than pure NF-Ni$_3$S$_2$ and NF-Ni(OH)$_2$/MnO$_2$ further evidenced the intrinsic optimization of active sites on heterointerfaces. Accordingly, electrochemical impedance spectroscopy (EIS) of NF-Ni$_3$S$_2$/MnO$_2$, bare NF, NF-Ni$_3$S$_2$, and NF-Ni(OH)$_2$/MnO$_2$ were provided in Fig. 4d. Consistent with HER catalytic competence, NF-Ni$_3$S$_2$/MnO$_2$ possessed the smallest charge-transfer impedance (R_{ct}), indicating the fast electron transport of the fabricated hierarchical heterogeneous Ni$_3$S$_2$/MnO$_2$ nanoarrays. Moreover, the rapid decrease of R_{ct} value after conversion of NF-Ni(OH)$_2$/MnO$_2$ to NF-Ni$_3$S$_2$/MnO$_2$ suggested that the efficient improvement of material resistance was mainly attributed to the participation of Ni$_3$S$_2$, which had an outstanding intrinsic metallic conductivity. Considering that catalytic stability was served as another vital assessment criteria for catalytic practicability, the long-term stability test of NF-Ni$_3$S$_2$/MnO$_2$ was performed in 1.0 M KOH with commercial Pt/C as the reference. As shown in Fig. 4e, it could be learned that the Pt/C owned a superior initial HER activity but poor electrocatalytic durability. This could be that the Pt/C catalyst was easy to poisoning [53]. However, the prepared NF-Ni$_3$S$_2$/MnO$_2$ catalyst revealed an inconspicuous decrease in the current density after 48 h circulation. Moreover, NF-Ni$_3$S$_2$/MnO$_2$ expressed a negligible loss of cathode current after 10,000 cyclic test in the j-η curve. Both the phenomena confirmed the NF-Ni$_3$S$_2$/MnO$_2$ had satisfactory practicability.

In view of the fact that the amount of TAA vulcanizing agent determined the morphology and composition of the intertwined Ni$_3$S$_2$ and MnO$_2$ nanosheet hybrid arrays, this indicated that the catalytic activity of NF-Ni$_3$S$_2$/MnO$_2$ was closely related to the content of TAA. As displayed in Fig. S14a, the HER catalytic activity of Ni$_3$S$_2$/MnO$_2$ hybrid array changed with the TAA feeding amount and followed the rules of first enhancement and then attenuation. Moreover, the maximal activity was obtained when the molar weight of TAA was 3 mmol g (TAA-3). Obeying with the above regularity, an optimal Tafel slope (b = 69 mV dec^{-1}) were also gained in TAA-3 (Fig. S14b). As shown in Figs. S15 and S14c, although some very close and comparable C_{dl} were found in other samples, HER activity and Tafel slope were not as good as TAA-3. This result could be ascribed to the fact that sample TAA-3 had the best R_{ct} as confirmed by Fig. S14d. As summarized in Fig. 4f, a minimum η_{10} of 102 mV and a maximum C_{dl} of 118.3 mF cm^{-2} for NF-Ni$_3$S$_2$/MnO$_2$ was obtained at the optimum TAA-3 feed. This clearly proved the accelerated exposure of Ni$_3$S$_2$/MnO$_2$ active interfaces on graded hybrid nanoarrays.

The OER activity of the NF-Ni$_3$S$_2$/MnO$_2$ electrode along with NF-Ni(OH)$_2$/MnO$_2$, NF-Ni$_3$S$_2$, pure NF and commercial IrO$_2$ were also explored in 1 M KOH aqueous electrolyte. As exhibited in Fig. 5a, the linear sweep voltammetry (LSV) curves at a scan rate of 1 mV s^{-1} clearly manifested that NF-Ni$_3$S$_2$/MnO$_2$ controlled the maximum OER activity in those samples. Among them, NF-Ni$_3$S$_2$/MnO$_2$ electrode afforded a current density of 10 mA cm^{-2} at a small overpotential (η_{10}) of 260 mV for the OER. However, 327, 342, 392 and 307 mV overpotentials were required for NF-Ni(OH)$_2$/MnO$_2$, NF-Ni$_3$S$_2$, pure NF and commercial IrO$_2$/C to achieve the corresponding current densities, respectively. Moreover, it just needed around 348 mV overpotential to drive a high current density of 100 mA cm^{-2}, which was far superior to most previously reported electrode materials (Table S3) [24,45,54–66]. Meanwhile, the Tafel slope of NF-Ni$_3$S$_2$/MnO$_2$ in Fig. 5b was only
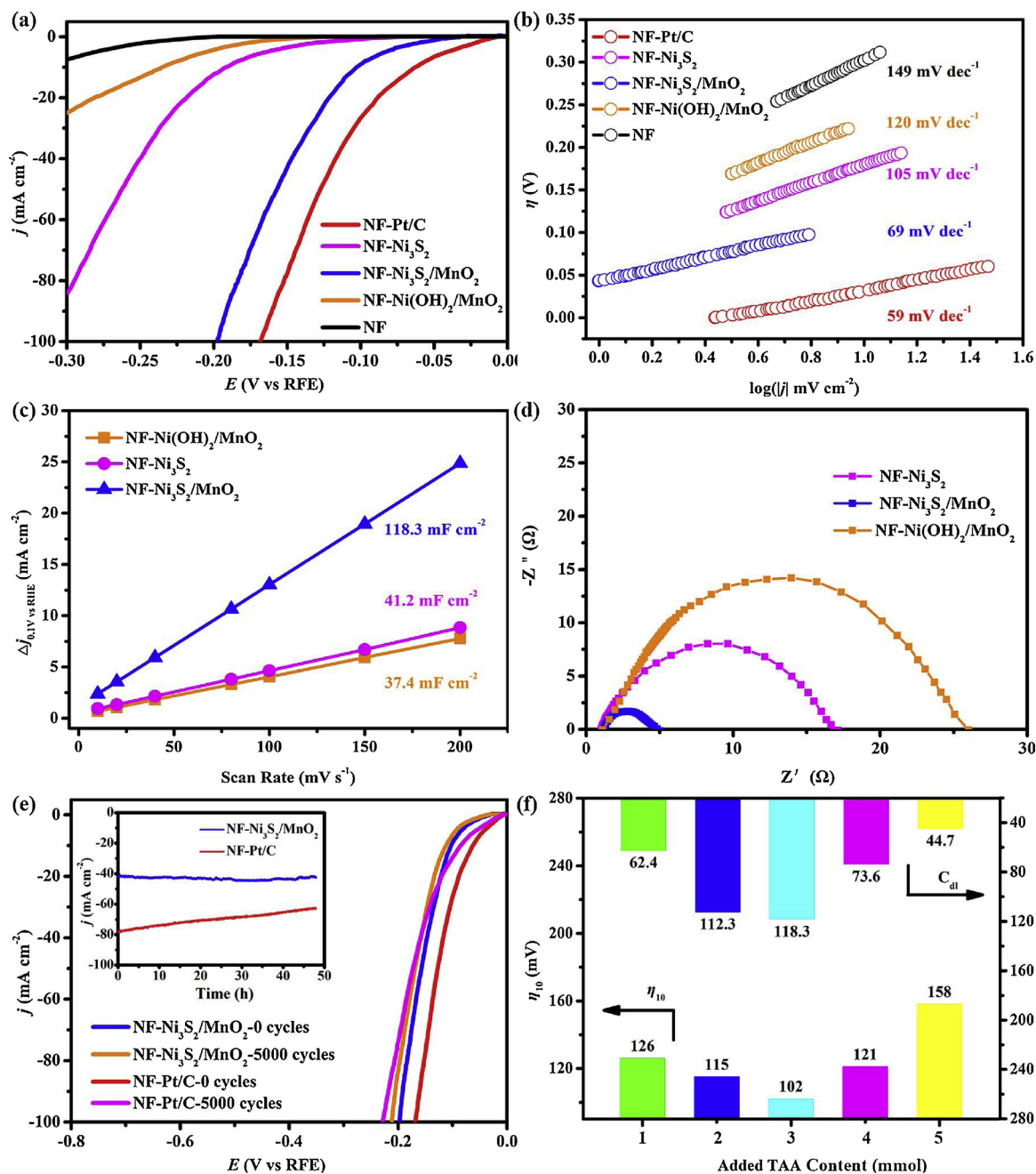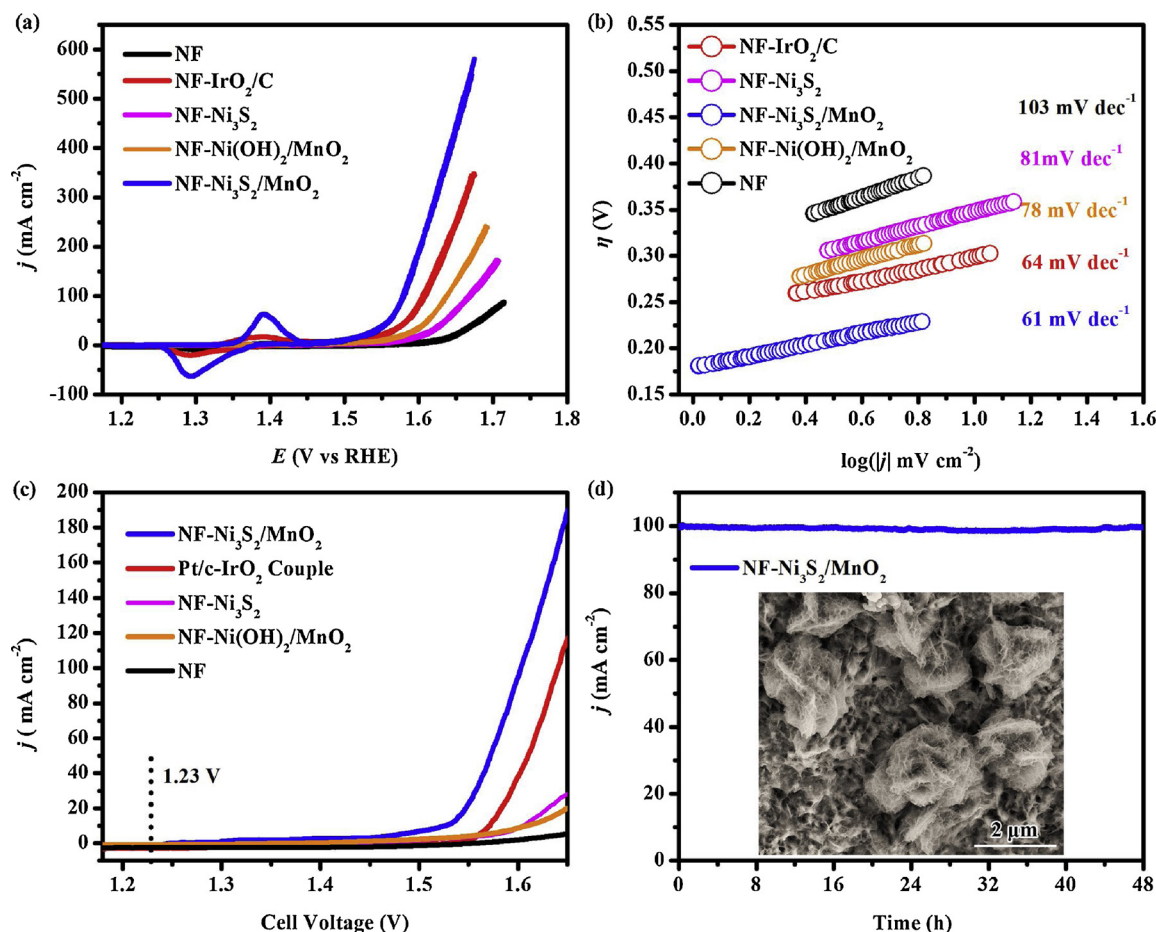
Fig. 4. (a) Polarization curves and (b) Tafel plots of NF, NF-Ni$_3$S$_2$, NF-Ni(OH)$_2$/MnO$_2$, NF-Ni$_3$S$_2$/MnO$_2$, and NF-Pt/C. (c) C_{dl} and (d) Nyquist plots (at $\eta = 150$ mV) of NF-Ni$_3$S$_2$, NF-Ni(OH)$_2$/MnO$_2$, NF-Ni$_3$S$_2$/MnO$_2$. (e) Stability detection of NF-Ni$_3$S$_2$/MnO$_2$, and NF-Pt/C. (f) η_{10} and C_{dl} values of various NF-Ni$_3$S$_2$/MnO$_2$ samples.

61 mV dec^{-1}, which was clearly smaller than that of the other four electrodes (NF-Ni(OH)$_2$/MnO$_2$: 78 mV dec^{-1}, NF-Ni$_3$S$_2$; 81 mV dec^{-1}, NF: 103 mV dec^{-1} and IrO$_2$: 64 mV dec^{-1}). Similar to the analysis in HER, the OER current of NF-Ni$_3$S$_2$/MnO$_2$ normalized by C_{dl} in Fig. S16 was obviously higher than pure NF-Ni$_3$S$_2$, also confirming the intrinsically enhanced activity was tightly associated with the synergy between Ni$_3$S$_2$ and MnO$_2$ nanosheets. Furthermore, the chronoamperometry (CP) curves at an initial current density of 100 mA cm^{-2} were tested to assess the cycling stability of the prepared NF-Ni$_3$S$_2$/MnO$_2$ electrode (Fig. S17a). It did not seem to fluctuate significantly after 36 h of examination. Combined with the OER catalytic activity that almost the same as the initial phase after 5000 consecutive cycles inside of Fig. S17b, it enabled to affirm that the as-synthesized NF-Ni$_3$S$_2$/MnO$_2$ also possessed an excellent OER catalytic stability. Noteworthily, the stability of NF-Ni$_3$S$_2$/MnO$_2$ in basic media was also much

better than that of IrO$_2$. As displayed in Fig. S17a, the commercial IrO$_2$ lost its activity for OER by ~30% only after 10 h. Considering the excellent electrocatalytic HER and OER activity of NF-Ni$_3$S$_2$/MnO$_2$ in 1 M KOH, the designed NF-Ni$_3$S$_2$/MnO$_2$ heterogeneous electrode in this work was reasonable and might be served as a highly efficient catalyst for electrocatalytic overall water splitting.

As revealed in Fig. S18, NF-Ni$_3$S$_2$/MnO$_2$ was further utilized as bifunctional electrocatalysts to realize the overall water splitting of the two-electrode system. Significantly, it afforded a 10 mA cm^{-2} current density at an applied voltage of 1.52 V (a combined overpotential of ~290 mV) using 1.0 M KOH as the electrolyte (Fig. 5c). Such activity of NF-Ni$_3$S$_2$/MnO$_2$ surpassed the commercial IrO$_2$-Pt couple (~1.57 V at 10 mA cm^{-2}) and other previously demonstrated overall water splitting catalysts (Table S4) [8,2,24,36,67–78], such as MoS$_2$-Ni$_3$S$_2$ nanoparticles (1.56 V), Ni$_3$FeN/g-GO aerogel (1.60 eV), Ni$_3$Se$_2$ nanoforest/

Fig. 5. (a–b) CV curves and Tafel plots of NF, NF-Ni$_3$S$_2$, NF-Ni(OH)$_2$/MnO$_2$, NF-Ni$_3$S$_2$/MnO$_2$, and NF-IrO$_2$/C for OER in 1.0 M KOH. (c) Polarization curves of NF, NF-Ni$_3$S$_2$, NF-Ni(OH)$_2$/MnO$_2$, NF-Ni$_3$S$_2$/MnO$_2$, and NF-IrO$_2$/C for overall water splitting in 1.0 M KOH. (d) Long-term durability test of NF-Ni$_3$S$_2$/MnO$_2$ at 1.6 V for overall water splitting in 1.0 M KOH. Inside: SEM image of NF-Ni$_3$S$_2$/MnO$_2$ after 48 h hydrolytic dissociation.

Ni foam (1.61 V), Ni-Co-P HNBs (1.2 V), N-NiMoO$_4$/NiS$_2$ nanowires/nanosheets (1.60 V), and the like. More fortunately, NF-Ni$_3$S$_2$/MnO$_2$ heterogeneous arrays submitted outstanding durability with a negligible reduction over a 48 h galvanostatic electrolysis at 100 mA cm^{-2} (Fig. 5d). Compared with the commercial noble metal IrO$_2$-Pt couple (gradually lost its activity), the fabricated NF-Ni$_3$S$_2$/MnO$_2$ heterogeneous electrode was clearly dominant. Additionally, the remained hierarchical nanostructures of NF-Ni$_3$S$_2$/MnO$_2$ arrays after 48 h cycle test further demonstrated its excellent durability (Figs. 5d and S19). The crystal structure of the catalyst was examined by XRD (Fig. S20), and some characteristic peaks of nickel-based oxides were found, which should be attributed to the conversion of Ni$_3$S$_2$ to the (oxy)hydroxide active species on the original surface during the electrochemical test. Further HRTEM analysis (Fig. S21) confirmed the above results, in which the newly emerging d-spacing of 2.1 nm was attributed to the (200) phase of the NiO active species. On the other hand, the total water splitting ability of NF-Ni$_3$S$_2$/MnO$_2$ at high current density (100 mA cm^{-2} at 1.6 V) was also conducted. As stated in Fig. S22, a large number of bubbles were detected on the two electrodes having a single-cell AAA Ni-Zn battery of 1.6 V. Refer to the above superior results, the establishing of NF-Ni$_3$S$_2$/MnO$_2$ electrolyzer was of research significance.

3.3. Electrocatalytic mechanism of NF-Ni$_3$S$_2$/MnO$_2$

To better understand the synergistic effect of Ni$_3$S$_2$ and MnO$_2$ heterojunction interface on electrocatalytic overall water splitting, the key reaction steps of alkaline HER and OER at Ni$_3$S$_2$, MnO$_2$, and Ni$_3$S$_2$/

MnO$_2$ interface were studied by DFT calculation [57,79–81]. It was well known that the alkaline HER reaction pathways involved dissociation of H$_2$O (Volmer step) as well as the adsorption and recombination of H* (Heyrovsky and Tafel steps), wherein H$_2$O dissociation was the first rate-determining step [69,71]. Moreover, alkaline OER pathways included a four-electron transfer pathway, in which the rate-limiting step was typically depended on the generation of *O from *OH (ΔG3) or the production of *OOH from *O (ΔG4) [58,76]. The overall water splitting process for Ni$_3$S$_2$/MnO$_2$ simulated by the computer was followed in Fig. 6a. Correspondingly, the relevant HER and OER reaction pathways for single Ni$_3$S$_2$ and MnO$_2$ were presented in Figs. S23–S24. The optimized free energy diagrams for alkaline HER and OER were calculated and the correlative Gibbs free energies were summarized in Tables S5–S7. As shown in Fig. 6b, the activated water adsorption energy (ΔG$_{H2O}$) and the binding free energies of H* intermediates (ΔG$_{H*}$) for Ni$_3$S$_2$ in HER were as high as 0.77 eV and 0.56 eV, respectively. Those big values implied its poor alkaline HER activity, which was in great agreement with the actual inspection of NF-Ni$_3$S$_2$ in Fig. 4a. Exhilaratingly, an apparent improvement of Ni$_3$S$_2$ in HER kinetics was exposed after Ni$_3$S$_2$ coupled with MnO$_2$. The values of ΔG$_{H2O}$ and ΔG$_{H*}$ for Ni$_3$S$_2$/MnO$_2$ were as lower as 0.24 eV and -0.03 eV (Fig. 6c), respectively. The result suggested that the construction of Ni$_3$S$_2$/MnO$_2$ heterogeneous interface immensely facilitated the adsorption of H$_2$O on catalyst surface as well as the cleaving of H−OH bonds, achieving the efficient evolution of H$_2$ [49,79]. As revealed in Fig. 6d and Table S7, it could be known that the rate-limiting steps for the three samples in alkaline OER were ΔG4, considering that the OER activity was determined by the maximum Gibbs free energy barrier [53,58]. Luckily,
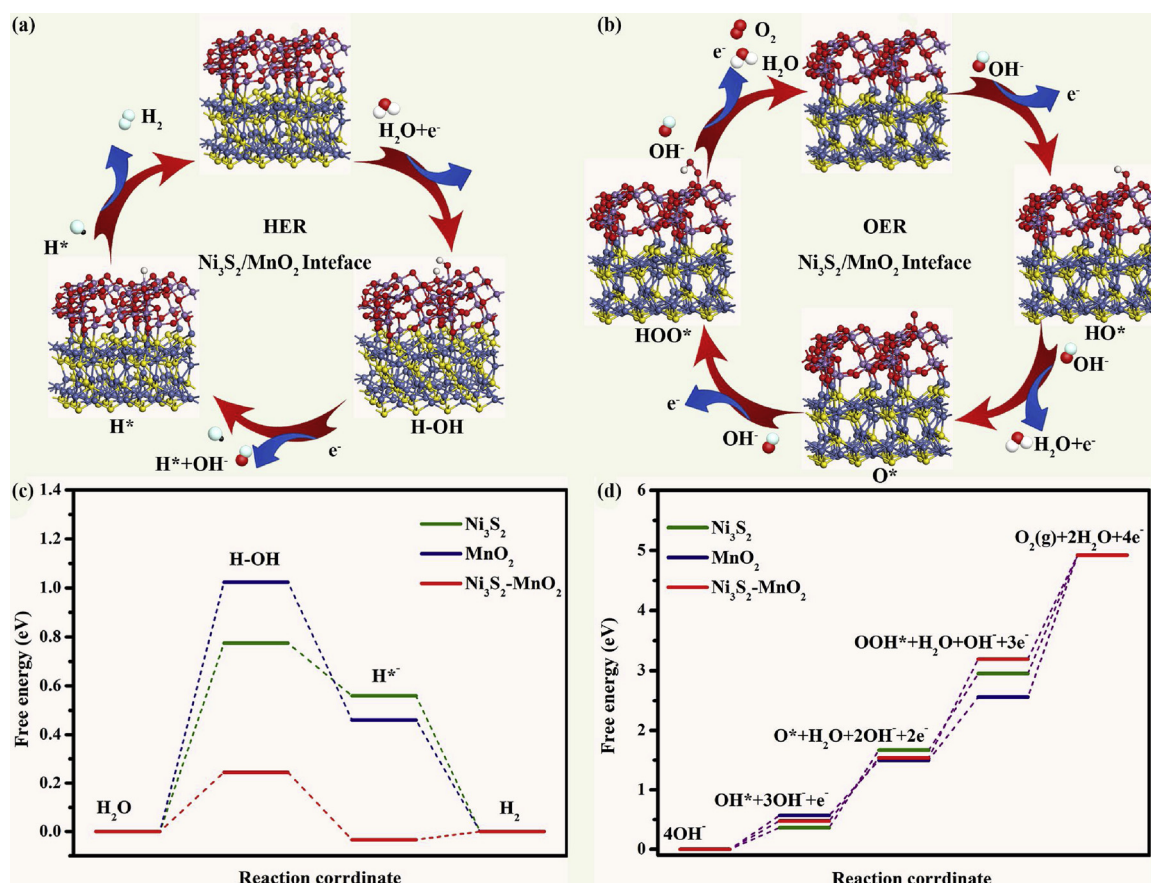
Fig. 6. (a) Schematic illustration of water activation, H* intermediate formation and hydrogen generation processes on NF-Ni_3S_2/MnO_2 hybrid catalyst in 1.0 M KOH. (b) Schematic illustration of OH^- activation, OH*/O*/OOH* generation and oxygen formation processes on NF-Ni_3S_2/MnO_2 hybrid catalyst in 1.0 M KOH. (c, d) Calculated reaction energy diagram at different stages of H_2O dissociation toward H_2 and O_2 generation in 1.0 M KOH.

the $\Delta G4$ value was greatly reduced from the 0.74 for Ni_3S_2 or 1.12 for MnO_2 to the final 0.49 for Ni_3S_2/MnO_2. The little $\Delta G4$ demonstrated the hybridization of Ni_3S_2/MnO_2 was conducive to alkaline OER, which was consistent with the experimental test. In brief, both experimental and theoretical results indicated that the effective adsorption and cleavage of H_2O molecule on the catalyst surface caused by the heterogeneous interface was the reason for the excellent total hydrolysis performance of the NF-Ni_3S_2/MnO_2 catalyst. In summary, the excellent catalytic performance of NF-Ni_3S_2/MnO_2 for overall water decomposition could be ascribed to the following reasons: (i) Superior intrinsic metallic conductivity of Ni_3S_2. (ii) Hierarchical structures of ultrathin nanosheet assembly. (iii) Construction of heterogeneous interfaces with highly efficient mass transfer performance. (iv) Participation with robust half-metallic MnO_2 nanosheets.

4. Conclusion

In conclusion, atomically thin nanosheet heterogeneous array of NF-Ni_3S_2/MnO_2 was successfully constructed via a facile two-step hydrothermal conversion. The hierarchical heterogeneous arrays of NF-Ni_3S_2/MnO_2 with abundant active heterointerfaces perfectly integrated and optimized the advantages of both several layered Ni_3S_2 and MnO_2, achieving the desired fast kinetics and outstanding performance for overall water decomposition in alkaline condition. For alkaline HER and OER, it was capable of realizing a 10 mA cm^{-2} current density at a low overpotential of 98 mV and 152 mV, respectively. More importantly, for overall water splitting in 1.0 M KOH, it required only 1.6 V of battery voltage to achieve a large current density of 100 mA cm^{-2}, exceeding most existing non-noble metal catalysts and even the Pt/C-IrO_2/C couple. DFT analysis evidenced that such

excellent electrocatalytic performance could be due to the effective adsorption and cleavage of H_2O molecule on the catalyst surface caused by the high-exposure hierarchical heterogeneous interface. In a word, this work opens up new opportunities for non-precious metal hydrolyzed electrocatalysts through the development of Ni-Mn based electrocatalysts with reasonable interface and nanostructures.

Appendix A. Supplementary data

Supplementary material related to this article can be found, in the online version, at doi:https://doi.org/10.1016/j.apcatb.2019.05.017.

References

[1] Y. Xu, M. Kraft, R. Xu, Metal-free carbonaceous electrocatalysts and photocatalysts for water splitting, Chem. Soc. Rev. 45 (2016) 3039–3052.
[2] S. Dutta, A. Indra, Y. Feng, H. Han, T. Song, Promoting electrocatalytic overall water splitting with nanohybrid of transition metal nitride-oxynitride, Appl. Catal. B-Environ. 241 (2019) 521–527.
[3] J. Yin, Y. Li, F. Lv, Q. Fan, Y.-Q. Zhao, Q. Zhang, W. Wang, F. Cheng, P. Xi, S. Guo, NiO/CoN porous nanowires as efficient bifunctional catalysts for Zn–air batteries, ACS Nano 11 (2017) 2275–2283.
[4] B. You, N. Jiang, M. Sheng, S. Gul, J. Yano, Y. Sun, High-performance overall water splitting electrocatalysts derived from cobalt-based metal–organic frameworks, Chem. Mater. 27 (2015) 7636–7642.
[5] Y. Liu, S. Jiang, S. Li, L. Zhou, Z. Li, J. Li, M. Shao, Interface engineering of (Ni, Fe)

$S_2@MoS_2$ heterostructures for synergetic electrochemical water splitting, Appl. Catal. B-Environ. 247 (2019) 107–114.

[6] Q. Xu, H. Jiang, H. Zhang, Y. Hu, C. Li, Heterogeneous interface engineered atomic configuration on ultrathin $Ni(OH)_2/Ni_3S_2$ nanoforests for efficient water splitting, Appl. Catal. B-Environ. 242 (2019) 60–66.

[7] J. Yin, Y. Li, F. Lv, M. Lu, K. Sun, W. Wang, L. Wang, F. Cheng, Y. Li, P. Xi, S. Guo, Oxygen vacancies dominated NiS_2/CoS_2 interface porous nanowires for portable Zn–air batteries driven water splitting devices, Adv. Mater. 29 (2017) 1704681.

[8] L. An, J. Feng, Y. Zhang, R. Wang, H. Liu, G.-C. Wang, F. Cheng, P. Xi, Epitaxial heterogeneous interfaces on N-$NiMoO_4/NiS_2$ nanowires/nanosheets to boost hydrogen and oxygen production for overall water splitting, Adv. Funct. Mater. 29 (2019) 1805298.

[9] Z. Kang, H. Guo, J. Wu, X. Sun, Z. Zhang, Q. Liao, S. Zhang, H. Si, P. Wu, L. Wang, Y. Zhang, Engineering an earth-abundant element-based bifunctional electrocatalyst for highly efficient and durable overall water splitting, Adv. Funct. Mater. 0 (2019) 1807031.

[10] L. An, Z. Zhang, J. Feng, F. Lv, Y. Li, R. Wang, M. Lu, R.B. Gupta, P. Xi, S. Zhang, Heterostructure-promoted oxygen electrocatalysis enables rechargeable zinc–air battery with neutral aqueous electrolyte, J. Am. Chem. Soc. 140 (2018) 17624–17631.

[11] L. An, J. Feng, Y. Zhang, Y.-Q. Zhao, R. Si, G.-C. Wang, F. Cheng, P. Xi, S. Sun, Controllable tuning of Fe-N nanosheets by Co substitution for enhanced oxygen evolution reaction, Nano Energy 57 (2019) 644–652.

[12] B. You, Y. Sun, Innovative strategies for electrocatalytic water splitting, Acc. Chem. Res. 51 (2018) 1571–1580.

[13] Y. Pei, Y. Ge, H. Chu, W. Smith, P. Dong, P.M. Ajayan, M. Ye, J. Shen, Controlled synthesis of 3D porous structured cobalt-iron based nanosheets by electrodeposition as asymmetric electrodes for ultra-efficient water splitting, Appl. Catal. B-Environ. 244 (2019) 583–593.

[14] P.W. Menezes, C. Panda, S. Loos, F. Bunschei-Bruns, C. Walter, M. Schwarze, X. Deng, H. Dau, M. Driess, A structurally versatile nickel phosphite acting as a robust bifunctional electrocatalyst for overall water splitting, Energy Environ. Sci. 11 (2018) 1287–1298.

[15] M.A.R. Anjum, M.S. Okyay, M. Kim, M.H. Lee, N. Park, J.S. Lee, Bifunctional sulfur-doped cobalt phosphide electrocatalyst outperforms all-noble-metal electrocatalysts in alkaline electrolyzer for overall water splitting, Nano Energy 53 (2018) 286–295.

[16] G. Peng, J. Albero, H. Garcia, M. Shalom, A water-splitting carbon nitride photo-electrochemical cell with efficient charge separation and remarkably low onset potential, Angew. Chem. 130 (2018) 16033–16037.

[17] J. Peng, X. Chen, W.-J. Ong, X. Zhao, N. Li, Surface and heterointerface engineering of 2D MXenes and their nanocomposites: insights into electro- and photocatalysis, Chemistry 5 (2019) 18–50.

[18] W. He, G. Zhao, P. Sun, P. Hou, L. Zhu, T. Wang, L. Li, X. Xu, T. Zhai, Construction of Longan–like hybrid structures by anchoring nickel hydroxide on yolk–shell polypyrrole for asymmetric supercapacitors, Nano Energy 56 (2019) 207–215.

[19] X. Zhao, P. Pachfule, S. Li, J.R.J. Simke, J. Schmidt, A. Thomas, Bifunctional electrocatalysts for overall water splitting from an iron/nickel-based bimetallic metal–organic framework/dicyandiamide composite, Angew. Chem. 130 (2018) 9059–9064.

[20] Y. Meng, P. Sun, W. He, B. Teng, X. Xu, Uniform P doped Co–Ni–S nanostructures for asymmetric supercapacitors with ultra-high energy densities, Nanoscale 11 (2019) 688–697.

[21] C. Wang, P. Sun, G. Qu, J. Yin, X. Xu, Nickel/cobalt based materials for super-capacitors, Chin. Chem. Lett. 29 (2018) 1731–1740.

[22] H. Wang, J. Zhang, X. Hang, X. Zhang, J. Xie, B. Pan, Y. Xie, Half-metallicity in single-layered manganese dioxide nanosheets by defect engineering, Angew. Chem. 127 (2015) 1211–1215.

[23] Y. Zhao, C. Chang, F. Teng, Y. Zhao, G. Chen, R. Shi, G.I.N. Waterhouse, W. Huang, T. Zhang, Defect-engineered ultrathin δ-MnO_2 nanosheet arrays as bifunctional electrodes for efficient overall water splitting, Adv. Energy Mater. 7 (2017) 1700005.

[24] Y. Yang, K. Zhang, H. Lin, X. Li, H.C. Chan, L. Yang, Q. Gao, MoS_2–Ni_3S_2 hetero-nanorods as efficient and stable bifunctional electrocatalysts for overall water splitting, ACS Catal. 7 (2017) 2357–2366.

[25] J. Kibsgaard, Z. Chen, B.N. Reinecke, T.F. Jaramillo, Engineering the surface structure of MoS_2 to preferentially expose active edge sites for electrocatalysis, Nat. Mater. 11 (2012) 963.

[26] M.A. Lukowski, A.S. Daniel, F. Meng, A. Forticaux, L. Li, S. Jin, Enhanced hydrogen evolution catalysis from chemically exfoliated metallic MoS_2 nanosheets, J. Am. Chem. Soc. 135 (2013) 10274–10277.

[27] C.-L. Tang, X. Wei, Y.-M. Jiang, X.-Y. Wu, L.N. Han, K.-X. Wang, J.-S. Chen, Cobalt-doped MnO_2 hierarchical yolk–shell spheres with improved supercapacitive performance, Phys. Chem. C 119 (2015) 8465–8471.

[28] Y. Liu, Y. Qiao, W. Zhang, H. Wang, K. Chen, H. Zhu, Z. Li, Y. Huang, Nanostructured alkali cation incorporated δ-MnO_2 cathode materials for aqueous sodium-ion batteries, J. Mater. Chem. A 3 (2015) 7780–7785.

[29] L.-L. Feng, G. Yu, Y. Wu, G.-D. Li, H. Li, Y. Sun, T. Asefa, W. Chen, X. Zou, High-index faceted Ni_3S_2 nanosheet arrays as highly active and ultrastable electro-catalysts for water splitting, J. Am. Chem. Soc. 137 (2015) 14023–14026.

[30] D. Yan, Y. Liu, Y. Li, R. Zhuo, Z. Wu, Y. Ren, S. Li, J. Wang, P. Yan, Z. Geng, Synthesis and electrochemical properties of MnO_2/rGO/PEDOT:PSS ternary composite electrode material for supercapacitors, Mater. Lett. 127 (2014) 53–55.

[31] J. Li, W. Zhao, F. Huang, A. Manivannan, N. Wu, Single-crystalline $Ni(OH)_2$ and NiO nanoplatelet arrays as supercapacitor electrodes, Nanoscale 3 (2011) 5103–5109.

[32] Y. Wu, G.-D. Li, Y. Liu, L. Yang, X. Lian, T. Asefa, X. Zou, Electrocatalysis: overall

[33] water splitting catalyzed efficiently by an ultrathin nanosheet-built, hollow Ni3S2-based electrocatalyst, Adv. Funct. Mater. 26 (2016) 4999–4999.

[33] J. Tang, J. Min, P. Yuan, Y. Fu, X. Ma, Large-area, ultrathin inorganic network coverages–graphene hierarchical electrodes for flexible, heat-resistant energy storage application, Adv. Energy Mater. 6 (2016) 1600146.

[34] S.M. Wellman, J.R. Eles, K.A. Ludwig, J.P. Seymour, N.J. Michelson, W.E. McFadden, A.L. Vazquez, T.D.Y. Kozai, A materials roadmap to functional neural interface design, Adv. Funct. Mater. 28 (2018) 1701269.

[35] C. Xie, X.-T. Lu, X.-W. Tong, Z.-X. Zhang, F.-X. Liang, L. Liang, L.-B. Luo, Y.-C. Wu, Recent progress in solar-blind deep-ultraviolet photodetectors based on inorganic ultrawide bandgap semiconductors, Adv. Funct. Mater. 0 (2019) 1806006.

[36] J. Zhang, T. Wang, D. Pohl, B. Rellinghaus, R. Dong, S. Liu, X. Zhuang, X. Feng, Interface engineering of MoS_2/Ni_3S_2 heterostructures for highly enhanced electrochemical overall-water-splitting activity, Angew. Chem. 128 (2016) 6814–6819.

[37] W. He, C. Wang, H. Li, X. Deng, X. Xu, T. Zhai, Ultrathin and porous $Ni_3S_2/CoNi_2S_4$ 3D-network structure for superhigh energy density asymmetric supercapacitors, Adv. Energy Mater. 7 (2017) 1700983.

[38] B. Bai, J. Li, J. Hao, 1D-MnO_2, 2D-MnO_2 and 3D-MnO_2 for low-temperature oxidation of ethanol, Appl. Catal. B-Environ. 164 (2015) 241–250.

[39] T.A. Shifa, F. Wang, K. Liu, K. Xu, Z. Wang, X. Zhan, C. Jiang, J. He, Engineering the electronic structure of 2D WS_2 nanosheets using Co incorporation as $Co_xW_{(1-x)}S_2$ for conspicuously enhanced hydrogen generation, Small 12 (2016) 3802–3809.

[40] C. Tang, H. Zhang, K. Xu, Q. Hu, F. Li, C. He, Q. Zhang, J. Liu, L. Fan, Scalable synthesis of heterostructure molybdenum and nickel sulfides nanosheets for efficient hydrogen generation in alkaline electrolyte, Catal. Today 316 (2018) 171–176.

[41] Z. Wang, H. Du, Z. Liu, H. Wang, A.M. Asiri, X. Sun, Interface engineering of a CeO_2–Cu_3P nanoarray for efficient alkaline hydrogen evolution, Nanoscale 10 (2018) 2213–2217.

[42] L. Zheng, W. Hu, X. Shu, H. Zheng, X. Fang, Ultrafine CoP_x nanoparticles anchored on nitrogen doped reduced graphene oxides for superior hydrogenation in alkaline media, Adv. Mater. Interfaces 5 (2018) 1800515.

[43] T. Kou, T. Smart, B. Yao, I. Chen, D. Thota, Y. Ping, Y. Li, Theoretical and experimental insight into the effect of nitrogen doping on hydrogen evolution activity of Ni_3S_2 in alkaline medium, Adv. Energy Mater. 8 (2018) 1703538.

[44] Y. Ou, W. Tian, L. Liu, Y. Zhang, P. Xiao, Bimetallic $Co_2Mo_3O_8$ suboxides coupled with conductive cobalt nanowires for efficient and durable hydrogen evolution in alkaline electrolyte, J. Mater. Chem. A 6 (2018) 5217–5228.

[45] Z.H. Ibupoto, A. Tahira, P. Tang, X. Liu, J.R. Morante, M. Fahlman, J. Arbiol, M. Vagin, A. Vomiero, MoSx@NiO composite nanostructures: an advanced non-precious catalyst for hydrogen evolution reaction in alkaline media, Adv. Funct. Mater. 0 (2018) 1807562.

[46] S. Li, C. Cheng, A. Sagaltchik, P. Pachfule, C. Zhao, A. Thomas, Metal-organic precursor–derived mesoporous carbon spheres with homogeneously distributed molybdenum carbide/nitride nanoparticles for efficient hydrogen evolution in alkaline media, Adv. Funct. Mater. 29 (2019) 1807419.

[47] C. Tang, N. Cheng, Z. Pu, W. Xing, X. Sun, NiSe nanowire film supported on nickel foam: an efficient and stable 3D bifunctional electrode for full water splitting, Angew. Chem. 127 (2015) 9483–9487.

[48] Y. Feng, X.-Y. Yu, U. Paik, Nickel cobalt phosphides quasi-hollow nanocubes as an efficient electrocatalyst for hydrogen evolution in alkaline solution, Chem. Commun. 52 (2016) 1633–1636.

[49] M. Ledendecker, G. Clavel, M. Antonietti, M. Shalom, Highly porous materials as tunable electrocatalysts for the hydrogen and oxygen evolution reaction, Adv. Funct. Mater. 25 (2015) 393–399.

[50] L. Feng, H. Vrubel, M. Bensimon, X. Hu, Easily-prepared dinickel phosphide (Ni_2P) nanoparticles as an efficient and robust electrocatalyst for hydrogen evolution, Phys. Chem. Phys. 16 (2014) 5917–5921.

[51] D. Liu, Q. Lu, Y. Luo, X. Sun, A.M. Asiri, $NiCo_2S_4$ nanowires array as an efficient bifunctional electrocatalyst for full water splitting with superior activity, Nanoscale 7 (2015) 15122–15126.

[52] H. Vrubel, X. Hu, Molybdenum boride and carbide catalyze hydrogen evolution in both acidic and basic solutions, Angew. Chem. 124 (2012) 12875–12878.

[53] M. Martin-Martinez, A. Álvarez-Montero, L.M. Gómez-Sainero, R.T. Baker, J. Palomar, S. Omar, S. Eser, J.J. Rodriguez, Deactivation behavior of Pd/C and Pt/C catalysts in the gas-phase hydrodechlorination of chloromethanes: structure--reactivity relationship, Appl. Catal. B-Environ. 162 (2015) 532–543.

[54] Q. Hu, X. Liu, C. Tang, L. Fan, X. Chai, Q. Zhang, J. Liu, C. He, High efficiency oxygen evolution reaction enabled by 3D network composed of nitrogen-doped graphitic carbon-coated metal/metal oxide heterojunctions, Electrochim. Acta 265 (2018) 620–628.

[55] R. Lin, T. Lin, J. Huang, X. Huang, Y. Liu, Hierarchical cobalt sulfide with vertical in-plane edge structure for enhanced electrocatalytic oxygen evolution reaction, Electrochim. Acta 281 (2018) 348–356.

[56] J.-H. Kim, D.H. Youn, K. Kawashima, J. Lin, H. Lim, C.B. Mullins, An active nanoporous Ni(Fe) OER electrocatalyst via selective dissolution of Cd in alkaline media, Appl. Catal. B-Environ. 225 (2018) 1–7.

[57] Y. Bi, Z. Cai, D. Zhou, Y. Tian, Q. Zhang, Q. Zhang, Y. Kuang, Y. Li, X. Sun, X. Duan, Understanding the incorporating effect of Co^{2+}/Co^{3+} in NiFe-layered double hydroxide for electrocatalytic oxygen evolution reaction, J. Catal. 358 (2018) 100–107.

[58] B.K. Kim, S.-K. Kim, S.K. Cho, J.J. Kim, Enhanced catalytic activity of electrodeposited Ni-Cu-P toward oxygen evolution reaction, Appl. Catal. B-Environ. 237 (2018) 409–415.

[59] S. Fu, J. Song, C. Zhu, G.-L. Xu, K. Amine, C. Sun, X. Li, M.H. Engelhard, D. Du, Y. Lin, Ultrafine and highly disordered Ni_2Fe_1 nanofoams enabled highly efficient

oxygen evolution reaction in alkaline electrolyte, Nano Energy 44 (2018) 319–326.

[60] P. Feng, X. Cheng, J. Li, X. Luo, Co$_3$(PO$_4$)$_2$ nanoparticles embedded in nitrogen-doped carbon as an advanced electrocatalyst for OER in alkaline solution, Cataly. Lett. 148 (2018) 214–219.

[61] B. Kim, A. Oh, M.K. Kabiraz, Y. Hong, J. Joo, H. Baik, S.-I. Choi, K. Lee, NiOOH exfoliation-free nickel octahedra as highly active and durable electrocatalysts toward the oxygen evolution reaction in an alkaline electrolyte, ACS Appl. Mater. Interfaces 10 (2018) 10115–10122.

[62] U. De Silva, J. Masud, N. Zhang, Y. Hong, W.P.R. Liyanage, M. Asle Zaeem, M. Nath, Nickel telluride as a bifunctional electrocatalyst for efficient water splitting in alkaline medium, J. Mater. Chem. A 6 (2018) 7608–7622.

[63] S. Zhao, M. Li, M. Han, D. Xu, J. Yang, Y. Lin, N.-E. Shi, Y. Lu, R. Yang, B. Liu, Z. Dai, J. Bao, Defect-rich Ni$_3$FeN nanocrystals anchored on N-doped graphene for enhanced electrocatalytic oxygen evolution, Adv. Funct. Mater. 28 (2018) 1706018.

[64] K. Fan, H. Chen, Y. Ji, H. Huang, P.M. Claesson, Q. Daniel, B. Philippe, H. Rensmo, F. Li, Y. Luo, L. Sun, Nickel–vanadium monolayer double hydroxide for efficient electrochemical water oxidation, Nat. Commun. 7 (2016) 11981.

[65] Z.-Q. Liu, G.-F. Chen, P.-L. Zhou, N. Li, Y.-Z. Su, Building layered Ni$_x$Co$_{2x}$(OH)$_{6x}$ nanosheets decorated three-dimensional Ni frameworks for electrochemical applications, J. Power Sources 317 (2016) 1–9.

[66] B.B. Li, Y.Q. Liang, X.J. Yang, Z.D. Cui, S.Z. Qiao, S.L. Zhu, Z.Y. Li, K. Yin, MoO$_2$–CoO coupled with a macroporous carbon hybrid electrocatalyst for highly efficient oxygen evolution, Nanoscale 7 (2015) 16704–16714.

[67] W.Q. Yang, Y.X. Hua, Q.B. Zhang, H. Lei, C.Y. Xu, Electrochemical fabrication of 3D quasi-amorphous pompon-like Co−O and Co−Se hybrid films from choline chloride/urea deep eutectic solvent for efficient overall water splitting, Electrochim. Acta 273 (2018) 71–79.

[68] A. Wu, Y. Xie, H. Ma, C. Tian, Y. Gu, H. Yan, X. Zhang, G. Yang, H. Fu, Integrating the active OER and HER components as the heterostructures for the efficient overall water splitting, Nano Energy 44 (2018) 353–363.

[69] M.A.R. Anjum, M.D. Bhatt, M.H. Lee, J.S. Lee, Sulfur-doped dicobalt phosphide outperforming precious metals as a bifunctional electrocatalyst for alkaline water electrolysis, Chem. Mater. 30 (2018) 8861–8870.

[70] B. Wang, C. Tang, H.-F. Wang, B.-Q. Li, X. Cui, Q. Zhang, Anion-regulated hydroxysulfide monoliths as OER/ORR/HER electrocatalysts and their applications in self-powered electrochemical water splitting, Small Methods 2 (2018) 1800055.

[71] E. Hu, Y. Feng, J. Nai, D. Zhao, Y. Hu, X.W. Lou, Construction of hierarchical Ni–Co–P hollow nanobricks with oriented nanosheets for efficient overall water splitting, Energy Environ. Sci. 11 (2018) 872–880.

[72] F. Yu, H. Zhou, Y. Huang, J. Sun, F. Qin, J. Bao, W.A. Goddard, S. Chen, Z. Ren, High-performance bifunctional porous non-noble metal phosphide catalyst for overall water splitting, Nat. Commun. 9 (2018) 2551.

[73] Y. Gu, S. Chen, J. Ren, Y.A. Jia, C. Chen, S. Komarneni, D. Yang, X. Yao, Electronic structure tuning in Ni$_3$FeN/r-GO aerogel toward bifunctional electrocatalyst for overall water splitting, ACS Nano 12 (2018) 245–253.

[74] S. Huang, Y. Meng, S. He, A. Goswami, Q. Wu, J. Li, S. Tong, T. Asefa, M. Wu, N−, O−, and S-tridoped carbon-encapsulated Co$_9$S$_8$ nanomaterials: efficient bifunctional electrocatalysts for overall water splitting, Adv. Funct. Mater. 27 (2017) 1606585.

[75] X. Zhao, P. Pachfule, S. Li, J.R.J. Simke, J. Schmidt, A. Thomas, Bifunctional electrocatalysts for overall water splitting from an iron/nickel-based bimetallic metal–organic framework/dicyandiamide composite, Angew. Chem. Int. Ed. 57 (2018) 8921–8926.

[76] B. You, N. Jiang, M. Sheng, M.W. Bhushan, Y. Sun, Hierarchically porous urchin-like Ni$_2$P superstructures supported on nickel foam as efficient bifunctional electrocatalysts for overall water splitting, ACS Catal. 6 (2016) 714–721.

[77] R. Xu, R. Wu, Y. Shi, J. Zhang, B. Zhang, Ni$_3$Se$_2$ nanoforest/Ni foam as a hydrophilic, metallic, and self-supported bifunctional electrocatalyst for both H$_2$ and O$_2$ generations, Nano Energy 24 (2016) 103–110.

[78] W. Ma, R. Ma, J. Wu, P. Sun, X. Liu, K. Zhou, T. Sasaki, Development of efficient electrocatalysts via molecular hybridization of NiMn layered double hydroxide nanosheets and graphene, Nanoscale 8 (2016) 10425–10432.

[79] B. Zhang, J. Liu, J. Wang, Y. Ruan, X. Ji, K. Xu, C. Chen, H. Wan, L. Miao, J. Jiang, Interface engineering: the Ni(OH)$_2$/MoS$_2$ heterostructure for highly efficient alkaline hydrogen evolution, Nano Energy 37 (2017) 74–80.

[80] L. Zhang, I.S. Amiinu, X. Ren, Z. Liu, G. Du, A.M. Asiri, B. Zheng, X. Sun, Surface modification of a NiS$_2$ nanoarray with Ni(OH)$_2$ toward superior water reduction electrocatalysis in alkaline media, Inorg. Chem. 56 (2017) 13651–13654.

[81] N.H. Kwon, M. Kim, X. Jin, J. Lim, I.Y. Kim, N.-S. Lee, H. Kim, S.-J. Hwang, A rational method to kinetically control the rate-determining step to explore efficient electrocatalysts for the oxygen evolution reaction, NPG Asia Mater. 10 (2018) 659–669.